

Synchrotron X-ray Diffraction and Reflection Studies of a Polymacromonomer Monolayer at the Air–Water Interface: Transition from Aligned Single Molecules to Homogeneous Layer

Heiko Ahrens,[†] Georg Papastavrou,^{†,§} Manfred Schmidt,[‡] and Christiane A. Helm^{*,†}

Institut für Physik, Ernst-Moritz-Arndt Universität, Friedrich-Ludwig-Jahn-Str. 16, D-17487 Greifswald, Germany, and Institut für Physikalische Chemie, Johannes-Gutenberg Universität, Jakob-Welder Weg 11, D-55099 Mainz, Germany

Received: November 4, 2003; In Final Form: January 31, 2004

Monolayers of polymacromonomers with poly(vinyl)pyridine side chains of different lengths, polyPVP_{20.8} and polyPVP_{46.7}, are studied at the air/water interface. Combination of reflection data and diffraction peaks allows the establishment of a structural model. In the expanded phase at pressures below approximately 15 mN/m, the side chains are adsorbed to the air/water interface, causing polymer backbone stretching and alignment of the single molecules. The in-plane peaks are due to the lateral electron density variation above and below the adsorption layer. The diameter of the flattened cylindrical molecules corresponds to twice the contour length of the side chains (25 and 12.5 nm, respectively) and decreases on monolayer compression by approximately 20%, due to side chain desorption. Additionally, side chain desorption causes monolayer thickening. Above the phase transition, the lateral order disappears. Obviously, the side chains of adjacent molecules mix and the monolayer is homogeneous.

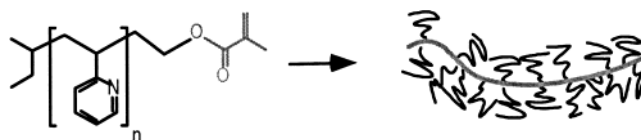
Introduction

Miniaturization of devices and control of interfacial properties draw modern research toward nanoscopic objects and low-dimensional systems such as single molecules and molecular layers. Information about the structure-properties relation can be extracted from deformation of single molecules, or even molecular groups.^{1,2,11,28} They provide insight into the molecular mechanisms of macroscopic processes which take place at interfaces, such as swelling, wetting, etc.

Cylindrical brushes represent regular comblike polymers with densely grafted side chains (cf. Scheme 1). They adopt a cylindrical conformation if the main chain is much longer than the side chains and if the repulsive interaction between the side chains is sufficiently high. Recently cylindrical brushes were reported to undergo a conformational transition from a cylindrical to a spherically collapsed shape upon external stimuli.²⁸ In these experiments, cylindrical brushes with poly(*n*-butylacrylate) side chains were spread on an LB trough forming monolayers. Upon compression of the monolayer, a transition of the cylindrical structure to collapsed globules was observed. More recently, cylindrical brushes with poly-*N*-isopropylacrylamide (PNIPAM) side chains were reported to undergo a single molecule cylinder to globule transition in dilute solution as well upon changing the temperature above the lower critical solution temperature of PNIPAM.¹⁹

Little is known so far how the directional persistence of cylindrical brushes changes, if confined to two dimensions and how adsorption of the side chains to a surface influences the

SCHEME 1: Structural Formulas of the Cylindrical Brushes PolyPVP_{20.8} and PolyPVP_{46.7} Obtained by Polymerization of the Macromonomers PVP_{20.8} and PVP_{46.7}



conformation. Theoretical considerations favor straightening of the polymer backbone upon adsorption of the side chains, though direct and convincing experimental evidence is still missing as side chain adsorption may also induce meander like conformations at least in the dry state.^{27,28}

In this paper, we focus on intermolecular and intramolecular interactions and on the ordering on the scale of several nanometers. As side chains, we use poly(vinyl)pyridine (PVP), which like poly(butyl acrylate) adsorbs onto the water surface. Previously, we investigated the layering transitions of polyPVP_{20.8} on the water surface.⁴ The cylindrical brush is swollen, therefore its shape transition is expected to be less pronounced than the one with poly(butylacrylate) side chains. Still, the polyPVP_{20.8} cylinders do not maintain their circular cross sections. At low coverage, their conformation is well described as flat cylinders with adsorbed side chains, whereas at high coverage, the cross-section is squeezed and a thicker monolayer results. Therefore, the forces of the two planar interfaces (water/cylinder and cylinder/air) are comparable in magnitude to the intra- and intercylinder interactions.⁴

For polyPVP the high one-dimensional anchoring density (1/2.5 Å⁻¹) results in a large side chain density close to the backbone, which increases the main chain persistence length. However, if not all side chains are adsorbed to the surface, the side chain density decreases with increasing distance from the

* To whom correspondence should be addressed. E-mail: helm@physik.uni-greifswald.de.

[†] Ernst-Moritz-Arndt Universität.

[‡] Johannes-Gutenberg Universität.

[§] New address: Department of Inorganic, Analytical and Applied Chemistry, University of Geneva, 30 Quai Ernest Ansermet, CH-1211 Geneva 4, Switzerland.

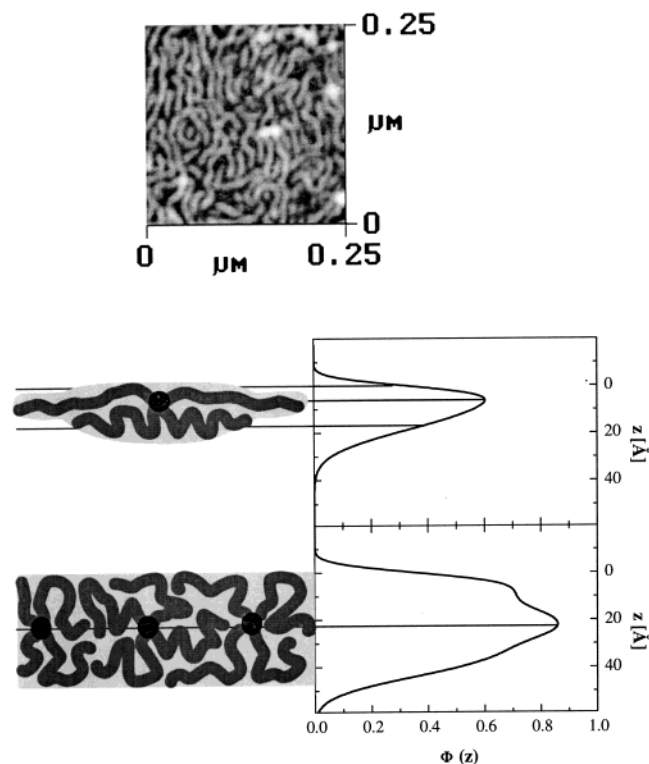


Figure 1. Top: AFM image of a PVP_{20.8} monolayer transferred at a molecular area of $\approx 250 \text{ \AA}^2/\text{macromonomer}$. On compressing beyond the phase transition at π_1 , i.e., at molecular areas below $\approx 160 \text{ \AA}^2/\text{macromonomer}$, it was impossible to observe any pattern (from ref 4). Bottom: Electron density profile as derived from X-ray reflectivity curves, together with a schematic drawing of cylindrical brush cross-section (top $232 \text{ \AA}^2/\text{macromonomer}$, bottom $101 \text{ \AA}^2/\text{macromonomer}$). The latter deviates from the schemes in ref 4, yet is consistent both with the reflectivity results⁴ and with the GID findings described in Figures 5 and 6.

backbone, which might influence the shape and deformability of the mesoscopic cylinders. Therefore, now we investigate polyPVP_{20.8} and a polymacromonomer with longer side-chains (polyPVP_{46.7}).

AFM and X-ray reflectivity measurements on the water surface⁴ suggest that the mesoscopic cylinders order in a stripe pattern, consistent with the straightening (cf. Figure 1) of the backbone, which might be further promoted by side chain adsorption. For polyPVP_{20.8}, AFM images of transferred monolayers and calculations based on X-ray reflectivity data⁴ suggest lattice distances between 50 and 120 \AA . Obviously, longer side chains will increase this distance.

Monolayers at the air/water interfaces are well suited to address such questions, because of the defined variability of parameters, especially the area per macromonomer. The system provides the additional advantage that surface energies can be assessed via surface tension measurements. Furthermore, monolayer equilibrium conformation is established in a much shorter time than on solid substrates. This technique has recently gained higher attention since the last two decades have seen a wealth of new technical developments, which allow the study of liquid interfaces at many length scales down to the molecular level.^{12,21}

Especially X-ray and neutron reflectivity measurements have proved most valuable to study the segment distribution perpendicular to the water surface, especially neutron reflectivity has gained outstanding relevance, since one may deuterate segments completely or partly and thus gain specific contrast.²⁹

However, due to limited flux in neutron scattering experiments, one cannot measure at high Q_z values as desirable. Measurement times are too long, and this limits the systematic variation of parameters. X-ray reflection measurements provide an alternative, due to the fact that even laboratory sources provide sufficient flux and Synchrotrons provide ample intensity. However, in most cases, scattering relies on electron density contrast, and in this respect, many polymers are not sufficiently distinguishable from water. A new development has been to increase the contrast via insertion of heavy counterions into the subphase.²

In the case of ordered arrangements, X-ray diffraction is known to be the most direct and precise technique of structure analysis. These measurements became possible also for the liquid/gaseous interface in the last 15 years by making use of the high brilliance of Synchrotron sources.¹⁶ With this technique an X-ray beam strikes the surface at grazing incidence (grazing incidence diffraction, GID) and assuming lateral periodicity of the atom density projected on the surface one observes Bragg peaks. The scattered intensity $I(Q)$ is measured as a function of the scattering vector $Q = (Q_x, Q_y, Q_z) = (Q_{x,y}, Q_z)$, with $Q_{x,y}$ as the horizontal and Q_z as the vertical scattering vector. There is no restriction on the z component of the Bragg scattered ray. A 2-D crystalline lattice confines the X-ray scattering vector to Bragg rods along the z direction and not to Bragg points as in the case of a 3-D crystal.

However, comparing mesoscopic cylindrical brushes to the small molecules for which GID has been developed, striking differences become obvious. The lattice spacing is not 5–10 \AA , but 1 or 2 orders of magnitude larger and may well exceed the monolayer thickness. Therefore, (i) the scattering vector for GID measurements has to be calculated exactly, and widely used approximations are not justified. Furthermore, (ii) the scattering geometry has to be adjusted to allow grazing incidence small-angle X-ray diffraction (GISAXD).^{3,22} (iii) The intensity of a Bragg rod at a particular Q_z value is determined by the square of the molecular structure factor $|F_{\text{mol}}(Q_z)|^2$. For small molecules, $|F_{\text{mol}}(Q_z)|^2$ is evaluated according to an atomic coordinate model of the molecules. Obviously, mesoscopic worms with a locally random side chain configuration cannot be described as laterally incompressible atoms or pseudoatoms consisting of groups of atoms. We will have to use a much coarser model of the average molecular structure in the unit cell, to obtain a laterally periodic electron density profile.

Experimental and Analysis

Polymacromonomers. Two different polymacromonomers were investigated (cf. Scheme 1): polyPVP_{20.8} is a polymacromonomer with PVP_{20.8} side chains and a poly(metacrylate) (PMMA) backbone and a molecular weight of $M_w = 2.5 \times 10^6 \text{ g/mol}$.⁴ PolyPVP_{46.7} has PVP_{46.7} side chains and $M_w = 4.2 \times 10^6 \text{ g/mol}$. For both molecules, the polydispersity is about two. Obviously, the length of the backbone exceeds the side chain length by at least a factor of 8.

Monolayer Preparation and Isotherms. The water used for all experiments was Millipore purified and deionized (18.2 M Ω cm). NaI was obtained from Merck. Chloroform solutions of the appropriate cylindrical brushes were spread over one of the two subphases: deionized water or 10 mMol NaI solution. The pressure was detected by a Wilhelmy balance. The Langmuir trough was enclosed in a gastight canister with X-ray transparent windows. The trough temperature was set to 20 $^\circ\text{C}$, and the equilibrium time after monolayer spreading was at least 30 min.

X-ray Techniques. The scattered X-ray intensity is proportional to the Fourier transform squared of the electron

density $\rho(x,y,z)$ in the scatterer

$I(Q) \propto$

$$\left| \int \int \int dy \, dz \exp(i(Q_x \cdot x + Q_y \cdot y + Q_z \cdot z)) \rho(x,y,z) \right|^2 \quad (1)$$

It is convenient to separately consider the consequences of eq 1 for horizontal and vertical scattering, i.e., X-ray reflectivity and Grazing Incidence Diffraction (GID).

X-ray Reflectivity. The X-ray reflectivity of a monolayer at the air/water interface is given as a function of the perpendicular scattering vector $Q_z = (4\pi/\lambda)\sin \alpha$, with α = incidence angle and λ the X-ray wavelength. The normalized reflectivity R/R_F depends on the laterally averaged electron density profile, $\rho(z)$. R_F is the Fresnel reflectivity of an ideally sharp interface between air and water ($\rho_{\text{sub}} = 0.334 \text{ e}/\text{\AA}^3$)²⁵

$$\frac{R(Q_z)}{R_F(Q_z)} = \left| \frac{1}{\rho_{\text{sub}}} \int \frac{d\rho(z)}{dz} e^{iQ_z \cdot z} dz \right|^2 \quad (2)$$

To derive the electron density profile $\rho(z)$ one has to use models. A successful strategy is to represent the monolayer as a stack of slabs, each with a constant density ρ_i and thickness l_i . The constant density of the semi-infinite subphase has to be added below the interface. Finally, the model density must be smeared out in the z direction to account for the intrinsic vertical roughness or diffuseness of the interfaces. The rms roughness, σ , is of the order of 3 Å and stems mainly from thermally excited capillary waves on the water surface. The rather large value ($\sigma \approx 3 \text{ Å}$) means that in the atomic model of $\rho(z)$ it is unnecessary to use accurate charge densities of the atoms. As long as each atom contributes its proper charge Z_i , the description will be adequate. The large value of σ is also the reason that the monolayer may be adequately represented by a slab model.

X-ray reflectivity measurements up to $Q_z = 0.4 \text{ Å}^{-1}$ were performed with a home-built setup described elsewhere.⁹ For high Q_z values, additional measurements have been performed at the synchrotron (at the beamline BW1 at HASYLAB, DESY, Hamburg, Germany) in the cases where the previous measurements indicated signals in that range.

Data Analysis. The electron density profile has been obtained by two complementary strategies:

(i) The electron density profile is determined with a model-independent method.^{23,24} From the experimentally observed reflectivity curve, the corresponding profile correlation function is estimated via indirect Fourier transformation. For this profile correlation function the matching electron density profile is then derived by square-root deconvolution. Both the correlation function and the density profile are expressed in terms of a linear combination of a set of suitable basis functions. The number of basis functions, and thus, that of free parameters, can be optimized (minimized) by a smoothness criterion for the correlation function and, in most cases, no a priori assumptions on the shape of the electron-density profile have to be made.

(ii) The slab model is used. The parameters are determined by least-squares methods. It is convenient, because it can be easily applied to eq 2 and individual slabs may be identified with certain structural properties of the layers.

Our interpretation of the reflectivity data was considered satisfactory when the scattering profiles resulting from the two different modeling processes were equivalent. To obtain structural parameters characterizing a monolayer in one phase, we used the slab model with the fewest and most independent parameters (interdependency analysis according to ref 8) with

which all reflectivity curves measured within one phase could be fitted satisfactorily.

Grazing Incidence X-ray Diffraction (GID). The GID measurements were performed at the liquid surface diffractometer, at the beamline BW1 in HASYLAB.¹⁸ The scattered intensity was detected by a position sensitive detector (PSD) equipped with Soller slits.

Then, the horizontal and vertical components of the scattering vector Q are

$$Q_{xy} = \frac{2\pi}{\lambda} \sqrt{\cos^2 \alpha_i + \cos^2 \alpha_f - 2 \cos \alpha_i \cos \alpha_f \cos 2\theta_{xy}} \quad (3)$$

$$Q_z = \frac{2\pi}{\lambda} (\sin \alpha_i + \sin \alpha_f) \quad (4)$$

α_i and α_f being the angle between the plane of the liquid surface and the incident and the diffracted beam, respectively, and $2\theta_{xy}$ being the angle between the incident and diffracted beams projected onto the horizontal (x,y) plane. To reduce the background of photons scattered from the subphase, the incidence angle α_i was set below the critical angle α_c for total external reflection: $\alpha_i = 0.85\alpha_c$. This limits the penetration to 50–100 Å.⁷ (If α_f would be a small angle in comparison to $2\theta_{xy}$, eq 3 would transform into the widely used approximation for small molecules, $Q_{xy} \approx (4\pi/\lambda)\sin \theta_{xy}$.)

The Q_{xy} positions of the Bragg peaks yield the lattice repeat distances

$$d = \frac{2\pi}{Q_{h,k}} \quad (5)$$

which can be indexed by two indices (h,k) to yield the unit cell ($Q_{xy} = Q^{h,k}$). There is no periodicity in the z direction; therefore, the scattering is concentrated along rods in reciprocal space. These “Bragg rods” are orthogonal to the monolayer and intercept the ($Q_z = 0$) plane at points $Q_{xy} = Q^{h,k}$ of the two-dimensional reciprocal lattice.

The measured intensity in z -direction is therefore only given by the molecular form factor

$$I_{h,k}(Q_z) \propto |F_{h,k}(Q_z)|^2 \quad (6)$$

In the past, this technique was mostly used for small molecules, like lipids or fatty acids. For these systems, the headgroups are disordered, and one basically measures the lateral order of aliphatic tails. Then, to calculate the “Bragg rods”, the aliphatic tails are replaced by pseudoatoms of length l , which can be described as incompressible cylinders. Vertically, the diffuseness and roughness of the interface smears the atom positions; therefore, the alkyl chain is adequately represented by an incompressible cylinder. Laterally, the cylinder position corresponds to the aliphatic tail position within the unit cell.¹⁷ Then, one obtains for the molecular form factor

$$F_{\text{mol}}(Q_z) = F_{h,k}(Q_z) \propto \frac{\sin\left(\frac{1}{2}lQ_z\right)}{Q_z} \quad (7)$$

Because the signal is obtained by averaging over many randomly distributed domains one basically observes a two-dimensional powder pattern. The detector resolves the vertical component of the X-ray scatter vector, Q_z . The lateral resolution is limited to that of the Soller slit (0.09° full width half-maximum). To avoid intensity from the specular reflected beam in the PSD, the width of the horizontal slit before the sample (S2 in ref 6)

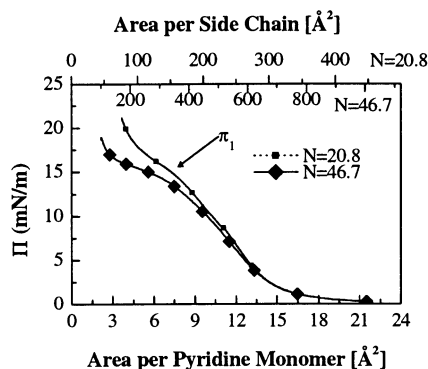


Figure 2. Isotherms of polyPVP_{20.8} and polyPVP_{46.7}, normalized per pyridine monomer (bottom x axis). As top x axis, the area per side chain monomer for the respective polymacromonomers is displayed.

was reduced to 1 or 0.5 mm. For the same reason, the horizontal slit (S3 in ref 6) directly before the Soler was reduced to 1 mm. To determine setup related background scattering, measurements without structured monolayers were performed.

The diffraction data are represented by a 2-D intensity distribution plot, showing the diffracted intensity $I(Q_{x,y}, Q_z)$ as a function of $Q_{x,y}$ and Q_z . The peaks are fitted by Gaussians in $Q_{x,y}$, and the full width at half-maximum (fwhm) yields the correlation length ξ in the surface plane associated with the h, k reflection according to¹⁷

$$\xi = \frac{1.6\pi}{\text{fwhm}(Q^{h,k})} \quad (8)$$

Experimental Results

Isotherms. Figure 2 presents the isotherms of polyPVP_{20.8} and polyPVP_{46.7}, which are both normalized to the area per pyridine monomer. The isotherms of the two different polymacromonomers almost superimpose. Nonzero pressure occurs at 17 Å²/pyridine (350 Å²/macromonomer and 800 Å²/macromonomer, respectively) and the lateral pressure increases rather steeply. At $\pi_1 \approx 15$ mN/m (7.5 Å²/pyridine, corresponding to 150 Å²/macromonomer and 350 Å²/macromonomer,

respectively), the pronounced change in slope indicates a phase transition.⁵ In the case of much further compression, eventually the pressure increases again, which was shown to lead to layering transitions.⁴

Addition of 0.01 mol/L NaI to the aqueous subphase leads to a slight pressure increase in the isotherm (cf. Figure 3), whereas the general shape remains unaffected. Light scattering investigations of partially quaternized PVP in aqueous solution revealed that the solvent quality increases with increasing NaI above 0.4 mol/L. It was concluded that NaI represents a hypothetically good solvent for the polymer. Thus, preferential absorption of NaI to the PVP brush may occur. Alternatively, formation of I⁻ may lead to charge-transfer complexes which also would increase the concentration of iodine within the brush.¹⁰

For AFM measurements, the monolayer was compressed on the water surface to a selected macromonomer area and then transferred onto solid support.⁴ Note that the ordered stripe phase (cf. Figure 1) was only observed, if an expanded monolayer was used, with a lateral pressure below π_1 . Beyond the phase transition, the transferred monolayer appears totally homogeneous.

X-ray Reflectivity. X-ray reflectivity curves along the isotherm of polyPVP_{46.7} are shown in Figure 3a. For large macromonomer areas, the subphase contained 0.01 mol/L NaI. The iodine addition improves the contrast; therefore, two interference maxima could be observed, even for high macromonomer areas (curves α, β, χ). Upon monolayer compression, the maxima shift to smaller Q_z values, indicating film thickening. Additionally, up to two more interference maxima appear. Detailed analysis reveals that the interference extrema are equidistant (except for the most compressed curves δ and ϵ). The centers of these oscillations constitute a very broad maximum, corresponding to a slow oscillation. The total film thickness can be deduced from the fast oscillations. Additionally, a thin yet high-density slab at the air side is necessary to accommodate the broad maximum. In total, two slabs (for curves δ and ϵ three slabs) are necessary to simulate the electron density profile of the monolayer.

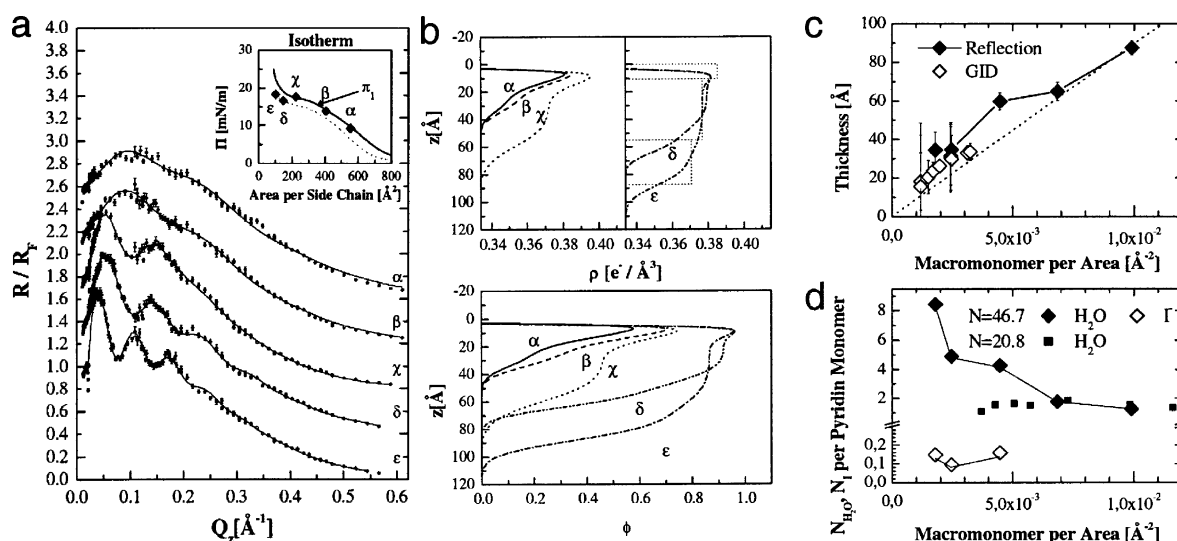


Figure 3. PolyPVP_{46.7} monolayers on 0.01 mol/L NaI (α, β, χ) and on water (δ, ϵ): (a) Normalized X-ray reflectivity R/R_F vs vertical scattering vector Q_z . The measurements are displaced vertically by 0.4 units and correspond to the surface pressures indicated ($\alpha, \beta, \chi, \delta, \epsilon$) in the inset. The dotted isotherm is measured on a clean water subphase, and the other is measured on the NaI subphase. (b) Best-fit density profiles $\rho(z)$ (top) and polymer volume fraction $\phi(z)$ (bottom) corresponding to the data ($\alpha, \beta, \chi, \delta, \epsilon$) of (a). Also shown is a schematic view of the parametrization of curve ϵ according to the slab model. (c) Monolayer thickness vs inverse macromonomer area A , calculated from the slab model (solid diamonds) and from GID according to eq 22 (open diamonds). (d) Incorporated iodine ions (open diamonds) and water molecules per pyridine monomer vs inverse macromonomer area A (solid diamonds). Hydration values of polyPVP_{20.8} from⁴ are given for comparison (squares).

TABLE 1: Parameters to Describe the Electron Density Profile of PolyPVP_{46.7}, as Derived from Least Square Fits for the X-ray Reflectivity Measurements Shown in Figure 3a

	area [Å ²]	π [mN/m]	l_1 [Å]	ρ_1 [e ⁻ /Å ³]	l_2 [Å]	ρ_2 [e ⁻ /Å ³]	l_3 [Å]	ρ_3 [e ⁻ /Å ³]	σ_{air} [Å]	σ_{sub} [Å]	L [Å]	$N_{\text{H}_2\text{O}}$	N_I
α	555 ^a	9.3	12.9	0.390	21.6	0.350			2.6		34.5	8.33	0.148
β	406 ^a	13.8	13.2	0.393	21.5	0.356			2.9		34.7	4.83	0.095
χ	223 ^a	17.7	13.6	0.406	46.2	0.372			3.3	11.4	59.8	4.17	0.157
δ	146	18.9	9.5	0.385	37.3	0.380	18.1	0.360	3.0	6.1	64.9	1.78	
ϵ	101	18.3	10.7	0.385	44.2	0.377	32.5	0.371	3.1	9.5	87.4	1.28	

^a Measurements on a 0.01 mol/L NaI solution, and the other experiments are performed on clean water. The electron density profile is parametrized by a slab model, with the air-adjacent slab as slab 1. Each slab is characterized by a thickness l_i , an electron density ρ_i and two interfacial roughnesses, $\sigma_{i-1,i}$ and $\sigma_{i,i+1}$. $L = l_1 + l_2$ ($L = l_1 + l_2 + l_3$, respectively) is the monolayer thickness, $N_{\text{H}_2\text{O}}$ and N_I represent the amount of water molecules and iodine ions per pyridine monomer, respectively. Always, the roughness between the first two slabs, $\sigma_{1,2}$, is chosen to be: $\sigma_{1,2} = l_1/2$. Additionally, the following constraints were applied: for experiments α, β : $\sigma_{\text{sub}} = \sigma_{1,2} = l_1/2$, and for δ, ϵ additionally $\sigma_{2,3} = l_3/2$.

The thus derived electron density profile $\rho(z)$ is shown in Figure 3b. A 12 ± 1.8 Å thick slab adjacent to the air interface exhibits the largest electron density within the monolayer. Upon compression, the electron density within each slab increases, and additionally, the monolayer part adjacent to the water thickens considerably (cf. Table 1). One obtains for the roughness of the monolayer/air interface a value of 3–4 Å, which is significantly smaller than 6–9 Å for the monolayer/water interface (cf. Figure 3c).

The monolayer electron density on the NaI subphase appears to be larger than on pure water, suggesting I^- incorporation. Both the amount of water molecules and iodine ions per pyridine monomer are calculated according to

$$V = Al = n_p V_p + n_I V_I + n_{\text{H}_2\text{O}} V_{\text{H}_2\text{O}} \quad (9)$$

$$E = Al\rho = n_p E_p + n_I E_I + n_{\text{H}_2\text{O}} E_{\text{H}_2\text{O}} \quad (10)$$

with A the area per macromonomer, l the monolayer thickness, ρ the average electron density; $V_p = 146$ Å³, $V_I = 58.1$ Å³, and $V_{\text{H}_2\text{O}} = 30$ Å³ are the molecular volumes of a pyridine monomer, an iodine ion, and a water molecule, respectively. E_p , E_I , and $E_{\text{H}_2\text{O}}$ are the corresponding number of electrons. $n_p = 46.7$ is the degree of polymerization per side chain. The water molecules $n_{\text{H}_2\text{O}}$ and the iodine ions n_I per macromonomer are calculated from eqs 9 and 10. n_I is found to be constant; it is equal to one iodine molecule per eight pyridine monomers, or 5.8 iodines per macromonomer.

To compare the electron density profiles of polyPVP_{46.7} obtained on the different subphases, the volume fraction profile of the polymer monomers is calculated by

$$\Phi(z) = \frac{\rho(z) - \rho_{\text{sub}} \text{erf}(z/\sigma)}{\rho_{\text{pol}} - \rho_{\text{sub}}} \quad (11)$$

where ρ_{sub} is the electron density of the subphase and ρ_{pol} is the density of either a monomer or a monomer and the appropriate amount of iodine. The error function accounts for the roughness of the liquid/gaseous interface. At large macromonomer areas, the side chains are swollen, and we observe eight water molecules per pyridine monomer (cf. Figure 3d). On compression, the swelling decreases, and eventually converges to 1.58 water molecules per pyridine monomer, almost the same value as found previously for polyPVP_{20.8}.⁴

In the examined pressure range, the thickness of the polyPVP_{46.7} varies by a factor of 2.5 (i.e., from 34.5 to 87.4 Å). The monolayer consisting of cylindrical brushes with short side chains, polyPVP_{20.8}, is thinner (between 15 and 53 Å,⁴), nevertheless the thickness variation is more pronounced (factor 3.5). Indeed, the monolayer thickness plotted vs the macromonomer/area shows a linear dependence, with a slope

corresponding to the hydrated macromonomer volume. The similarity between polyPVP_{46.7} and polyPVP_{20.8} becomes more obvious, when the monolayer thickness is normalized to the degree of side chain polymerization (cf. Figure 6b). The normalized thickness increases linearly, with a slope corresponding to the volume density of a hydrated monomer. One finds excellent agreement for both polyPVP_{20.8} and polyPVP_{46.7}.

Also, for both systems, and at molecular areas both below and above the phase transition at π_1 , the roughness at the polymer–air interface is significantly lower than the one at the polymer–water interface. This observation is consistent with the different interfacial tensions.

In the expanded state, the most striking feature of the density profile of polyPVP_{46.7} is the 12 ± 1.8 Å thick adsorption layer at the water surface. Its thickness is almost identical to the diameter of a PVP chain (10 Å⁴), suggesting a PVP adsorption layer. Comparing the reflectivity data of polyPVP_{20.8} and polyPVP_{46.7}, one notices differences. In the expanded phase, the hydration of the polyPVP_{20.8} appears to be constant. On compression, the thin and flattened cylinder is transformed into a thick and squeezed cylinder, and while the cylinder volume remains constant, obviously, the monomer hydration is unchanged, too. In contrast, at high molecular areas, the hydration of polyPVP_{46.7} appears to be larger, because the side chain density below the adsorption layer to the air/water interface is rather low, indicating very high hydration. In principle, the electron density profiles of both polymacromonomers at large pyridine areas are similar (cf. Figures 1 and 3 or 8): the density is largest close to the air interface, and then an extended decay toward the subphase occurs. Indeed, if the reflectivity curves of polyPVP_{20.8} are fitted by a two slab model similar to the one used to describe polyPVP_{46.7} at large macromonomer areas (in contrast to the one-slab model with two roughnesses, which is sufficient to describe the data⁴), i.e., a 12 Å thick air-adjacent adsorption layer and a water adjacent layer, one finds an increased molecular thickness and, consequently, a larger apparent hydration. Therefore, the differences between polyPVP_{20.8} and polyPVP_{46.7} below the phase transition at π_1 may be attributed to the limited resolution of X-ray reflectivity. The increase in hydration can be attributed either to an homogeneous, strongly swollen water adjacent layer, or alternatively to a laterally structured layer consisting of water and only weakly swollen polymer. The latter case will be discussed further down, after the diffraction data are described.

In the compressed state, beyond the phase transition at π_1 , there are unambiguous structural differences between polyPVP_{46.7} and polyPVP_{20.8}. The highest density of polyPVP_{46.7} is found at the air/polymer interface, and this can be attributed to preferential adsorption of the side-chains. The cylinder backbone cannot be identified within the polymer density profile. Appar-

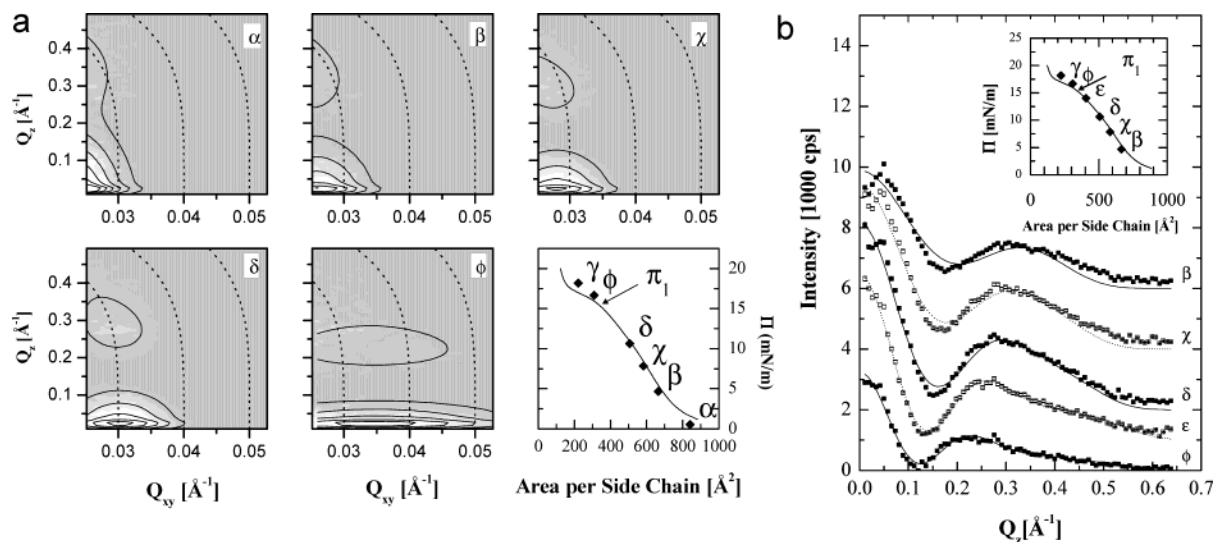


Figure 4. (a) Diffracted intensity for polyPVP_{46.7} monolayers on 0.01 mol/L NaI (contour plots, a.u.) in the Q_{xy} - Q_z plane. The slightly bend vertical lines give constant Q_{xy} . The measurements correspond to the surface pressures indicated (α , β , ...) in the isotherm. (b) Rod scans integrated for $0.025 < Q_{xy} < 0.055 \text{ \AA}^{-1}$. In both a and b, the lines indicate fits according to eq 21. No diffraction peaks were observed at point γ .

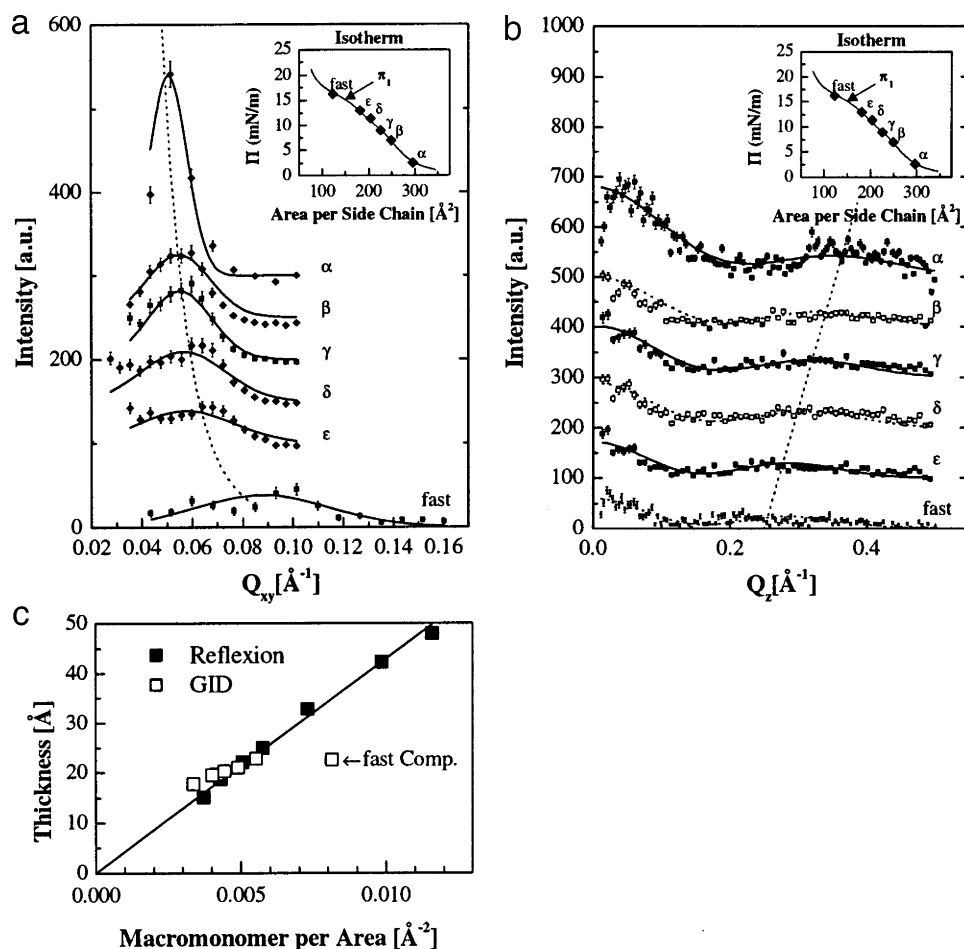


Figure 5. Diffracted intensity for polyPVP_{20.8} monolayers on pure water. (a) Intensity (integrated along the Bragg rod) vs Q_{xy} and (b) Bragg rods, i.e., intensity vs Q_z . For the latter plots, the intensity was integrated laterally, from all data points shown in part a. The solid lines are fits according to eq 22. The measurements correspond to the surface pressures indicated (α , β , ...) in the isotherm (inset to a). (c) Thickness of the ordered monolayer, extracted from the rod-scans data in b (open squares) and from the reflectivity measurements reported in Ahrens et al.⁴ (solid squares). The data point obtained by fast compression is indicated.

ently, the polymacromonomer backbones are not confined to the interface, but vertically distributed within the monolayer. In contrast, for poly PVP_{20.8}, the most dense slab is attributed to the cylinder backbone, it is sandwiched between two less

dense slabs (of equal thickness and density) containing side chains only⁴ (cf. Figure 1). No preferential adsorption to the air/water interface is found. Due to their high anchoring density, adjacent to the backbone the side chains are almost immobile.

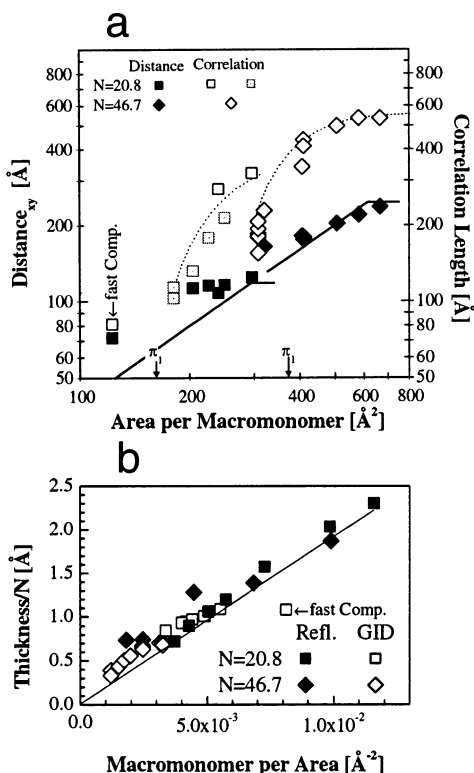


Figure 6. (a) Lattice spacing d and correlation length ξ for both polymacromonomers investigated. The phase transition as observed in the isotherm is indicated by π_1 . (b) Thickness l of the ordered monolayer, normalized relative to the degree of side chain polymerization, as determined from GID (open symbols) and from reflectivity data (solid symbols). Dotted lines in part a are guides to the eye, straight lines in part a were calculated according to $2r = A/a$ (see text for details), and straight lines in part b were calculated assuming constant cylinder volume.

Therefore, the vertical smearing of the backbone of the polyPVP_{46.7} can be attributed to the increased configurational freedom expected for longer side chains.

Grazing Incidence Diffraction. The diffracted intensity in the $Q_{x,y}$, Q_z plane for polyPVP_{20.8} and polyPVP_{46.7} monolayers on pure water is shown in Figures 4 and 5. (The slightly bent vertical lines represent constant $Q_{x,y}$ values, according to eq 3.) All plots start with the smallest $Q_{x,y}$ value, which was experimentally accessible in that specific alignment. Both the first and the second maximum of the rod-scan are resolved, always the maxima in Q_z occur at the same $Q_{x,y}$ value. At the onset of the lateral pressure increase, for both polymacromonomers, an in-plane peak is observed. Approaching π_1 , additionally the peak width ΔQ_{xy} increases, indicating a decrease in correlation length. Compressing slowly beyond π_1 , the peak disappears.

First, we will analyze the in-plane data, further down the rod-scans. On compression, the peak position shifts to larger $Q_{x,y}$ values, and the lattice distance decreases. The maximum lattice distance d for polyPVP_{20.8} and polyPVP_{46.7} is $d = 124$ and 250 Å, respectively, cf. Figures 4–6. These values are consistent with a lamellar structure, consisting of flat “cylinders” with totally stretched side chains: every $a = 2.5$ Å, a macromonomer with a contour length of $r_{\max} = 59$ Å ($r_{\max} = 123$ Å, respectively) is attached to the cylinder backbone. Therefore, the maximum diameter of the flattened “cylindrical” brush is $2r_{\max} = 118$ Å ($2r_{\max} = 246$ Å, respectively), which agrees well with the measured lattice distances.

The model of flat, aligned cylinders with totally stretched side chains is further supported, if one considers the isotherms. One obtains for the area per macromonomer $A = 2r_{\max} \cdot a = 310$ Å² ($2r_{\max} \cdot a = 696$ Å², respectively). Actually, the lateral pressure starts to increase at slightly larger macromonomer areas, 350 Å² (800 Å², respectively), probably due to the polydispersity and nonideal alignment of the cylindrical brushes. Note that even in the most expanded state the thickness of the monolayers exceeds the diameter of the PVP side chains (≈ 10 Å). This may be due to the fact that one measures the average thickness of a “carpet” consisting of adsorbed side chains and the rather thick backbone.

The lattice distance d for both polyPVP_{20.8} and polyPVP_{46.7} decreases by about 20%, from 124 to 99 Å (from 250 to 180 Å, respectively), cf. Fig. 6. Following our simple model, we calculate the cylinder diameter $2r$ from the macromonomer area A according to $2r = A/a$, i.e., the lattice distance decreases linearly with the molecular area. For each monolayer, the decrease is less than calculated. The deviations may be due to the simplicity of the model. Also defect annealing is ignored. In the monolayer of cylindrical brushes, many defects are likely because of the polydispersity of 2.5 of the cylinder length. Defect annealing is not new. It is also a prominent effect in lipid monolayers, and the decrease of the lattice distance is about a factor of 2 less than one would expect from the molecular area.¹⁴

Compressing the monolayer beyond π_1 , the flat region of the isotherm is reached. There, it was impossible to obtain a peak, suggesting a homogeneous monolayer. The rounded shape of the isotherm suggests a broad transition region. Actually, for PVP_{46.7}, it was possible to observe one peak after compressing slightly beyond π_1 , even though of drastically reduced intensity and decreased correlation length. Presumably, domains with pronounced electron density variations coexist with a homogeneous monolayer. On further compression, the peak disappears (cf. Figure 6a).

However, dynamic effects are important, too. This is obvious, if the results of different experiments are compared (cf. Figure 6a). Different monolayers exhibit slightly different peak positions, and compression/expansion cycles do not lead to entirely reproducible peaks. Annealing a monolayer for a few hours at a selected molecular area shifts the lattice distance to slightly larger values, and mostly it increases the integrated intensity (ca. factor 1.5). To explore memory effects, we compressed the polyPVP_{20.8} really fast (compression speed 16 Å²/min, time necessary to measure a peak 6 min, average speed 12 Å²/min) across the phase transition at π_1 and found one weak peak at a macromolecular area of 122 Å², and a correlation length corresponding to about one lattice distance. This peak beyond π_1 could not be observed in the case of slow compression (compression speed 10 Å²/min, time necessary to measure a peak 8 min, leading to an average speed of 3 Å²/min).

The correlation length is determined by the fwhm of the in-plane peaks according to eq 8 (cf. Figure 6b), yet the instrumental resolution is limited (0.09° corresponding to fwhm = $\Delta Q_{x,y} = 0.007$ Å⁻¹). Since for all experiments the fwhm exceeds the resolution by 20% (i.e., $\xi < 630$ Å), the correlation length ξ can be determined unambiguously after deconvolution. For both polymacromonomers, it is largest at the onset of the pressure increase (300 and 550 Å, respectively), it amounts to two to three lattice distances. Approaching π_1 , it decreases to about one lattice distance (150 and 100 Å, respectively). For polyPVP_{46.7}, the correlation length is almost constant, close to π_1 , and it decays fast. For polyPVP_{20.8}, two films were

investigated. One film exhibits similar behavior as the polymacromonomer with long side-chains (open squares in Figure 6a). The other film shows continuous decrease of the correlation length on compression (dotted squares in Figure 6a), but this monolayer was never allowed to achieve equilibrium configuration at zero pressure.

After analyzing the peaks in $Q_{x,y}$ and determining the lattice spacing and the correlation length, we now consider the rod-scans along Q_z (cf. Figures 4 and 5). They will yield information about the thickness of that slab within the monolayer, where lateral electron density variations occur. There are always two maxima, at $Q_{z,1} = 0$, and at larger $Q_{z,2}$. On compression, the second maximum $Q_{z,2}$ shifts to lower values (0.35 to 0.23 Å⁻¹ for polyPVP_{46.7} and 0.38 to 0.28 Å⁻¹ for polyPVP_{20.8}). For the polymacromonomer with the long side chains, polyPVP_{46.7}, the maximum position of the second-order peak occurs at lower Q_z values than for polyPVP_{20.8}.

According to eq 7, the condition for the first maximum is $Q_{z,1} = 0$, and for the second $Q_{z,2} \approx 3\pi/l$; that is, the position of the second order maximum is inversely proportional to the film thickness. Therefore, both the smaller $Q_{z,2}$ values for the molecule with longer side chains and the shift to lower $Q_{z,2}$ positions on film thickening are in good agreement with the predictions of eq 7. However, on detailed analysis, there are problems both with the position and the intensity of $Q_{z,2}$. The film thickness from GID is larger than the one determined by X-ray reflectivity (polyPVP_{46.7}: compressing from zero pressure to π_1 , GID and eq 7 yield a thickness change from 27 to 42 Å, maximum thickness according reflectivity: 35 Å. polyPVP_{20.8}: GID yields a thickness change from 23 to 30 Å, and X-ray reflectivity 15 to 25 Å). According to eq 7, the intensity of the second maximum should be reduced by a factor of $1/9\pi^2 = 0.033$; that is, it should be nearly 2 orders of magnitude smaller than the experimentally observed values shown in Figures 4a,b and 5b. Actually, the intensity of the $Q_{z,2}$ -peak amounts to 20–50% of the $Q_{z,1}$ peak. Therefore, we have to develop a model which is able to explain the observed diffracted intensity in the $Q_{x,y}$, Q_z plane and which furthermore is consistent with the monolayer thickness and the electron density profiles obtained by X-ray reflectivity.

Discussion

To find a suitable model for the ordered phase in the pressure range between 0 and 15 mN/m, we return to the reflectivity data. As explained above, the data analysis indicates flat or slightly squeezed cylinders lying on the water surface. To model the diffraction data (Figures 4 and 5), we need to calculate the structure factors for a lattice of deformed cylinders lying on a surface. By far the most scattering power resides in the electron density difference between the cylinders and the surroundings, i.e., water or air.

For a monolayer on a smooth substrate, the electron density $\rho_{\text{total}}(\mathbf{r})$ can be divided in a laterally homogeneous part, $\rho(z)$, and its local deviation $\rho_{\text{diff}}(x,y,z)$

$$\rho_{\text{total}}(\mathbf{r}) = \rho(z) + \rho_{\text{diff}}(x,y,z) \text{ with } \iint \rho_{\text{diff}}(x,y,z) dx dy = 0 \quad (12)$$

$\rho(z)$ determines according to eq 2 the specular reflected intensity, and $\rho_{\text{diff}}(x,y,z)$ determines the diffracted intensity.

The structure factor can be expressed as the Fourier transform of the local deviation of the electron density function

$$|F_{\text{mol}}(Q_{x,y} = Q^{h,k}, Q_z)|^2 = \left| \int_{\text{unit cell}} dx dy dz \exp(i\mathbf{Q}\mathbf{r}) \rho_{\text{diff}}(\mathbf{r}) \right|^2 = \left| \int_{\text{unit cell}} dz \exp(iQ_z z) \tilde{\rho}(z) \right|^2 \quad (13)$$

where $\tilde{\rho}(z)$ is the Fourier transform of the lateral electron density variation

$$\tilde{\rho}(Q_{x,y}, z) = \tilde{\rho}(z) = \iint_{\text{unit cell}} dx dy \exp(i(Q_x \cdot x + Q_y \cdot y)) \rho_{\text{diff}}(x,y,z) \text{ and } Q_{x,y} = Q^{h,k} \quad (14)$$

Traditionally, the chains of aliphatic tails molecules are described as cylinders stacked perpendicular to the surface. Then, one obtains

$$\tilde{\rho}(z) \propto \begin{cases} 1 & \text{if } -l/2 \leq z \leq l/2 \\ 0 & \text{elsewhere} \end{cases}$$

where l is the finite thickness of the ordered part of the monolayer. This yields again eq 7

$$|F_{\text{mol}}(Q_z)|^2 = |F_{h,k}(Q_z)|^2 \propto \left| \int_{-l/2}^{l/2} dz e^{iQ_z z} \right|^2 = 4 \frac{\sin^2\left(\frac{1}{2}lQ_z\right)}{Q_z^2} \quad (15)$$

Since in the present case the polymacromonomer cylinders are horizontally arranged on the air/water interface, instead of vertically stacked, one has to develop a different model. To begin with, we consider ideal, not deformed cylinders. Then, $\rho_{\text{diff}}(x,y,z)$ depends strongly on z . Furthermore, to evaluate the peak intensity, $\rho_{\text{diff}}(x,y,z)$ needs to be quantified. This is often not necessary for small amphiphilic molecules, but it is helpful to understand superstructure peaks. Let us consider $\rho_{\text{diff}}(x,y,z)$ at an arbitrary z_i value and a lateral structure in the x direction. If the lateral structure exhibits a periodicity of width d (cf. Figure 7), consisting of a stripe of width D with electron density ρ_1 and another stripe of width $(d - D)$ with electron density ρ_2 , because of $\iint dx dy \rho_{\text{diff}}(x,y,z) = 0$, one has to consider the following constraints:

$$D\rho_2 - (d - D)\rho_1 = 0 \quad (16)$$

and

$$\rho_1 - \rho_2 = \rho_{\text{Polymer}} - \rho_{\text{Surroundings}} \quad (17)$$

Therefore, one obtains for $\tilde{\rho}(z_i)$

$$\begin{aligned} \tilde{\rho}(z_i) &= \rho_1 \int_{-D/2}^{D/2} \exp(iQ_x \cdot x) dx + \rho_2 \left(\int_{-d/2}^{-D/2} \exp(iQ_x \cdot x) dx + \int_{D/2}^{d/2} \exp(iQ_x \cdot x) dx \right) = \\ &= \frac{(\rho_1 - \rho_2) \sin(Q_x \cdot D/2) + \rho_2 \sin(Q_x \cdot d/2)}{Q_x} = \\ &= \frac{(\rho_1 - \rho_2) \sin(Q_x \cdot D/2)}{Q_x} \text{ because of } Q_x = Q^{h,k} = 2\pi/d \quad (18) \end{aligned}$$

Note that $\tilde{\rho}(z_i)$ is largest when $Q_x \cdot D/2 = \pi/2$, i.e., $2D = d$. Obviously, one has maximum contrast, if the pattern forming the superstructure consists of two stripes with the same width. Furthermore, $\tilde{\rho}(z_i)$ increases with the difference in the electron density between polymer and surroundings. In the plane of the cylinder axis ($z = z_0$), the mesoscopic cylinders touch each other;

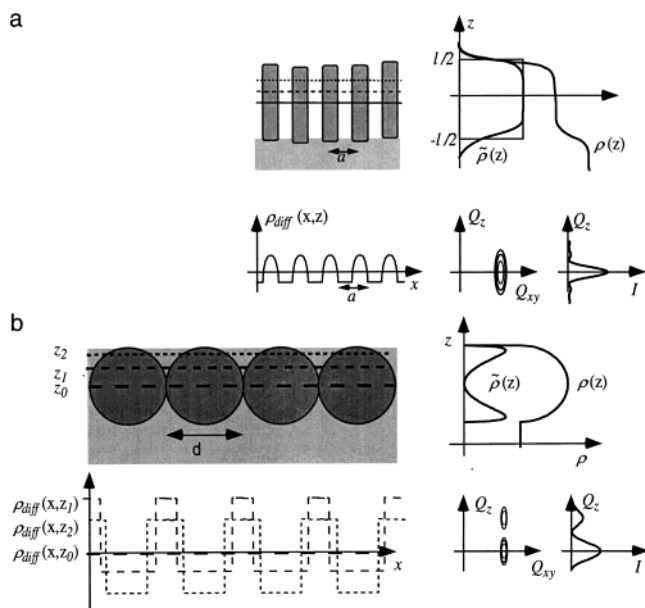


Figure 7. Model structures: (a) vertical and (b) horizontal cylinders. Top left: schematic view, bottom left: varying electron density $\rho_{\text{diff}}(x,z)$ along a Miller plane. Top right: average electron density profiles $\rho(z)$ together with its Fourier transform $\tilde{\rho}_{\text{diff}}$ at a peak position (i.e., $Q_{xy} = Q^{hk}$). Bottom right: schematic picture of Q_{xy} and Q_z plane. Bottom far right: calculated intensity along a Bragg rod (i.e. for $Q_{xy} = Q^{hk}$) vs Q_z (cf. eq 7 for part a and eq 21 for part b).

therefore, $\rho_{\text{diff}}(x,y,z_0) = 0$. Above and below the cylinder center, there is a strong modulation of the electron density. Because of the circular cross-section of the cylinder, we have an additional condition: $D^2 + (z - z_0)^2 = (d/2)^2$. Therefore, the Fourier transform of the in-plane electron density variation, $\tilde{\rho}(z)$, is given by (cf. Figure 7)

$$\tilde{\rho}(Q_{xy}, z) = (\rho_1 - \rho_2) \frac{\sin(Q_{xy} \sqrt{d^2/4 - (z - z_0)^2})}{Q_{xy}} \quad (19)$$

It exhibits a double peak at $z - z_0 = \pm d\sqrt{3}/4$ (cf. Figure 7). Thus one obtains a molecular structure factor which reads

$$F_{\text{mol}}(Q_z) \propto \frac{J_1(d\sqrt{Q_{xy}^2 + Q_z^2})}{\sqrt{Q_{xy}^2 + Q_z^2}} \text{ and } Q_{xy} = \frac{2\pi}{d} \quad (20)$$

where $J_1(a)$ is the first-order Bessel function. The thus calculated intensity distribution is shown in Figure 7. There are two peaks, one at $Q_z = 0$, and the second maximum for $Q_z > 0$ is only slightly weaker.

However, the shape of the polymacromonomer monolayers is akin to a deformed cylinder. Therefore, we need to deviate from the parameter-free model of perfect cylinders with circular cross-sections. The main features of $\tilde{\rho}(Q_{xy} = 2\pi/d, z)$ are maintained and are approximated by two Gaussian peaks above and below the contrast-free plane, which corresponds to the plane where the deformed cylinders are in contact. These two Gaussians are characterized by their widths w_1 and w_2 , and intensities A_1 and A_2 (both A_1 and A_2 depend on the variation of the electron density and the relative stripe width). The peak maxima are separated by a distance L

$$|F_{\text{mol}}(Q_z)|^2 \propto \left| \int_{-\infty}^{\infty} dz e^{iQ_z z} [A_1 e^{-(z-L/2)^2/2w_1^2} + A_2 e^{-(z+L/2)^2/2w_2^2}] \right|^2 = A_1^2 w_1^2 e^{-Q_z^2 w_1^2} + A_2^2 w_2^2 e^{-Q_z^2 w_2^2} + 2A_1 A_2 w_1 w_2 e^{-Q_z^2 (w_1^2 + w_2^2)/2} \cos(Q_z L) \quad (21)$$

The maximal lateral density variation occurs inside the monolayer and vanishes at the interfaces. Therefore, to obtain the monolayer thickness l^* , it is necessary to include the hwhm (half width half maximum) of the peaks

$$l^* = L + w_1 + w_2 \quad (22)$$

If the two peaks have identical widths w and same height (i.e., $A_1 = A_2 = 1$), eq 21 simplifies to

$$|F_{\text{mol}}(Q_z)|^2 \propto \left| \int_{-\infty}^{\infty} dz e^{iQ_z z} [e^{-(z-L/2)^2/2w^2} + e^{-(z+L/2)^2/2w^2}] \right|^2 = 4w^2 e^{-Q_z^2 w^2} \cos^2(Q_z L/2) \quad (23)$$

The latter formula is similar to the one of a double slit.¹³ Note that the intensity of the second maximum depends mainly on the width and the relative electron density of the ordered layers within the monolayer, and it can be much larger than eq 7 predicts for cylinders stacked perpendicular to the water surface. The position of the second maximum occurs according to eq 21 or eq 23 at $Q_{z,2} = 2\pi/L$.

The rod-scans of both polymacromonomers are fitted to eq 21. For the polymacromonomer with short side chains, polyPVP_{20.8}, the widths of the two peaks are chosen to be identical, and the least-squares fits find a slight difference between the peak amplitudes (cf. Table 3). (The peaks are too weak to justify a more elaborate data analysis).

For polyPVP_{46.7} (cf. Table 2), there is a larger difference of the fitted peaks in $\tilde{\rho}(Q_{xy} = 2\pi/d, z)$. One peak is very narrow ($w_1 \approx 1-2$ Å), with a large amplitude, and the other peak is broader and weaker by a factor of 4–6. The difference in lateral electron density variation appears to be very dramatic. At first, one might think that the electron density variation occurs beneath and above the cylinder backbone. However, the electron density profiles obtained by reflectivity measurements do not indicate that the cylinders touch each other at the backbones (cf. Figures 1 and 8), whereas they suggest a dense adsorption layer at the air/polymer interface and some side chains directly beneath the backbone.

To obtain such an intense second maximum in the rod scan as found experimentally, a pronounced minimum in the Fourier transform of the lateral electron density variation $\tilde{\rho}(Q_{xy} = 2\pi/d, z)$ is necessary. Since $\tilde{\rho}(Q_{xy} = 2\pi/d, z)$ vanishes, whenever the molecules touch and form a homogeneous layer, the adsorption layer at the polymer/air interface most likely provides the minimum. Below the adsorption layer, the side chains protruding into the subphase give the broad and weak maximum in the lower part of the $\tilde{\rho}(Q_{xy} = 2\pi/d, z)$ profile, as depicted in Figure 8.

The strong and narrow maximum on top of the adsorption layer can be attributed to the cylinder backbones protruding slightly out of the water. The difference in electron density of polymer and air is dramatic, explaining both the height and the small width of the peak in $\tilde{\rho}(Q_{xy} = 2\pi/d, z)$. Note that the structural roughness provided by the curved cylinder surface does not contribute much to the water/air roughness as measured with X-ray reflectivity, because the amplitude of the surface corrugation is about 1 Å and its wavelength a few 100 Å. The surface roughness of ~ 3 Å (cf. Table 1) as observed with X-ray

TABLE 2: Parameters as Derived from Least Square Fits for the GID Measurements of PolyPVP_{46.7} on 0.01 mol/L NaI Solution, According to Equation 21^a

	area [Å ²]	Q_{xy} [10^{-3} Å ⁻¹]	ΔQ_{xy} [10^{-3} Å ⁻¹]	distance d [Å]	correlation length ξ [Å]	w_1 [Å]	L [Å]	w_2 [Å]	A_1	A_2
β	665	26.6	12.2	236	534	1.1	14.5	4.8	22.4	2.4
χ	582	28.5	12.2	220	534	1.2	16.5	6.0	20.3	2.5
δ	507	31.0	12.8	203	496	1.6	18.6	6.0	15.5	2.7
	410	35.8	14.4	175	414	1.8	21.1	8.6	13.0	2.1
	410	35.3	13.9	178	437	1.7	20.7	8.4	13.6	2.1
	410	34.9	14.4	180	414	1.6	20.7	8.4	13.9	2.1
ϵ	406	34.7	16.6	181	342	1.8	21.6	6.3	11.4	2.7
	320	38.3	23.3	164	229	2.0	23.8	7.2	8.0	1.8
ϕ	308	34.8	33.3	181	155	2.2	24.3	7.1	6.5	1.5
	308	35.1	28.8	179	181	2.0	24.2	7.0	6.4	1.6
	308	34.1	27.2	184	193	1.8	23.6	6.9	7.2	1.7
	308	25.5	25.5	185	207	1.7	23.5	6.7	7.5	1.8

^a Those curves shown in Figure 4 are indicated by the respective letters. The Fourier transformed electron density variation of measurement ϵ is shown in Figure 8.

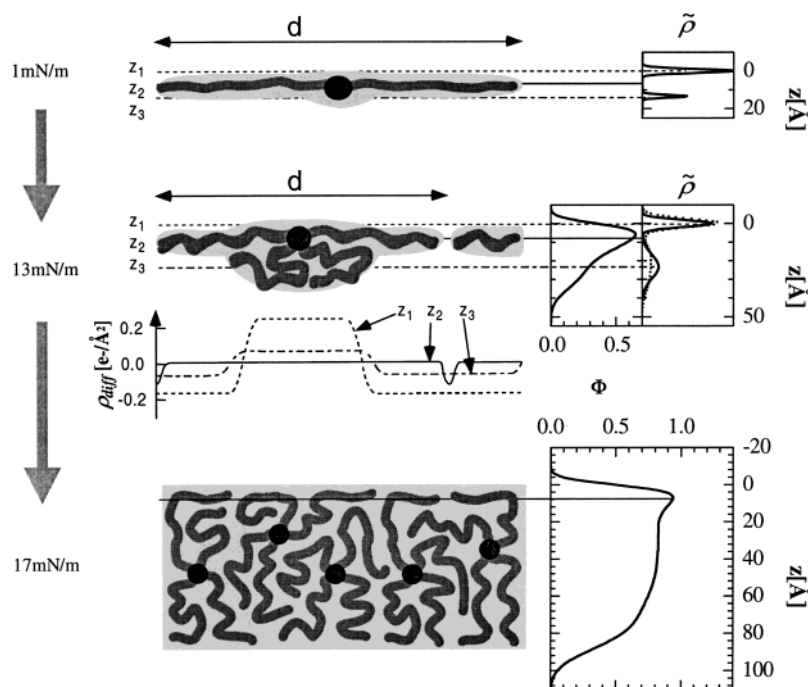


Figure 8. Scheme of a polyPVP_{46.7} monolayer at different molecular areas, together with volume fraction profile Φ , as calculated from electron density profiles (left, cf. Figure 3) and the Fourier transformed lateral electron density variation $\tilde{\rho}(Q_{xy}, z)$, if Bragg peaks could be observed (far right). At the onset of pressure increase (top, side chain area 890 Å²), the cylinder diameter corresponds to twice the side chain contour length. On compression, yet still in the expanded state (center, side chain area 406 Å²), a laterally almost homogeneous adsorption layer exists (at z_2). At this molecular area, about half the side chains are adsorbed to the air/water interface, as depicted. The adsorption layer induces a deformed monolayer/air interface (at z_1), and beneath, the polymer coils protrude into the water (at z_3). Both effects result in a laterally periodic electron density (left center) and provide the contrast for in-plane diffraction. Furthermore, from the volume fraction $\Phi(z)$, $\tilde{\rho}(Q_{xy}, z)$ is calculated with the assumptions described in the text (dashed line). Above the phase transition at an area per side chain of 350 Å², the backbone is vertically distributed and the side chains mix laterally, and no contrast for X-ray diffraction is available (bottom, side chain area 101 Å²).

reflectivity is dominated by capillary waves with long wavelengths (μm to mm , depending on the slit configuration), since they have the largest amplitude.²⁶

To cross-check this idea, $\tilde{\rho}(Q_{xy} = 2\pi/d, z)$ is calculated from the volume fraction $\Phi(z)$, also depicted in Figure 8. It is impossible to obtain the minimum of $\tilde{\rho}(Q_{xy} = 2\pi/d, z)$ observed experimentally. Only after multiplying $\Phi(z)$ with a factor of 1.4 to obtain a close-packed “carpet”, the minimum is obtained (cf. Figure 8). Simultaneously, the second broader peak is weaker than the one observed experimentally. (To calculate the polymer width $D(z)$ according to eq 16, the following additional assumptions are used: ρ_{polymer} is assumed to be constant, with a hydration of 1.6 water molecules per pyridine monomer, consistent with the reflectivity data, cf. Figures 6b. Above the maximum of $\Phi(z) = \Phi(z_{\text{max}})$; that is, above the polymer carpet, we have $\rho_{\text{surroundings}} = \rho_{\text{air}} = 0$, whereas below the maximum,

the monolayer is immersed in water, i.e., $\rho_{\text{surroundings}} = \rho_{\text{sub}} = 0.334 \text{ e}^-/\text{\AA}^3$.) Focusing on an ordered domain, the increased polymer density in the “carpet” is justified, because the backbone–backbone distance in the zero-pressure regime amounts to twice the side chain contour length, suggesting an extremely high side chain coverage in the ordered stripe phase. Both the AFM images and the rather low compressibility observed in GID suggest an extremely high defect density, which apparently decreases the average coverage in the “carpet”, as observed with X-ray reflectivity.

A further validation of the proposed model to explain the GID data is given by the comparison between the thickness l^* derived from diffraction (eq 22) with the thickness l obtained from reflection (cf. Figure 7b). For the macromolecule with short side chains, polyPVP_{20.8}, we find excellent agreement. For polyPVP_{46.7}, the diffraction and reflection results show also a

TABLE 3: Parameters as Obtained by Least Square Fits for the GID Measurements of PolyPVP_{20.8} on Pure Water, According to Equation 21^a

	area [Å ²]	Q_{xy} [10^{-3} Å ⁻¹]	ΔQ_{xy} [10^{-3} Å ⁻¹]	distance d [Å]	correlation length ξ [Å]	A_1	L [Å]	A_2
α	296	50.7	17.5	124	321	2.46	8.6	0.86
	240	58.5	19.7	107	278	2.67	10.7	1.05
fast	123	87.5	62.5	72	81	0.98	13.6	0.40
ϵ	181	56.9	45.0	110	113	0.98	13.7	0.42
β	249	54.1	24.7	116	214	1.34	10.5	0.64
χ	226	54.5	29.2	115	178	1.44	11.3	0.55
δ	204	55.8	39.0	113	132	1.23	12.0	0.47

^a Those curves shown in Figure 5 are indicated by the respective letters. Additionally, the constraint $w_1 = w_2 = 3.125$ Å was used.

good correspondence; nevertheless, they both exceed the expected thickness when one assumes a constant macromonomer volume (including hydration). This fact has been described above, and obviously, it can be attributed to the lateral structure within the monolayer.

By AFM (cf. Figure 1), an ordered stripe phase is observed only if the transfer occurs at lateral pressures below π_1 . If the monolayer is compressed beyond the phase transition, the transferred monolayer appears totally homogeneous. These findings are in very good agreement with the GID data and, furthermore, demonstrate that the monolayer maintains its molecular arrangement during transfer onto solid supports.

Concluding, combination of X-ray reflectivity and diffraction yields a very detailed structure of the single aligned molecules. At zero lateral pressure, the cylinder diameter is twice the side chain contour length; therefore, the angle between polymer backbone and every side chain is 90°. Furthermore, all side chains are stretched. On compression, we observe a decrease in cylinder separation and a repulsion between the aligned single molecules (i.e., increase of the lateral pressure).¹⁵ At this point, side chain desorption occurs, and more and more side chains are found beneath the cylinder backbone. Since the polymer concentration is increased beneath the backbones, a side chain appears to be adsorbed or desorbed, never partially adsorbed.

The length of the side chains does not influence the polymer conformation in the ordered phase, yet in the laterally homogeneous phase, the electron density profiles of the two polymacromonomer monolayers differ. In the case of short side chains (polyPVP_{20.8}), the cylinder backbones are all in the same surface plane; furthermore, the side chain distribution above and below the backbone is symmetric. For longer side chains (polyPVP_{46.7}), the backbones are vertically spread; additionally, a PVP adsorption layer directly at the water surface is found. Obviously, the detailed segment density profile in the disordered phase is of minor importance for the phase transition, which occurs at the same area per pyridine for both polymacromonomers. When the area per pyridine is reduced by a factor of 2, the side chains start to mix, and the monolayer becomes laterally homogeneous.

The less side chains are adsorbed, the smaller the intracylinder forces are which confine the cylinder backbone at the air–water interface and which cause molecular stretching. The phase transition occurs when the backbones desorb from the interface, and the side chains from different molecules interpenetrate and mix. Therefore, the phase transition is caused not only by intermolecular interactions as is known from polymers with a simple architecture but by intramolecular interactions, too.

It is intriguing to speculate about the nature of the phase transition at π_1 . With GID, we monitor the laterally periodic electron density profile, and do not observe directly the cylinder backbones. However, in the disordered phase, the persistence length of the cylinder backbone is decreased (the more the longer

the side chain length),^{28,27} which leads to the vertically spread backbones of polyPVP_{46.7}. Therefore, the phase transition at π_1 could indeed be a reentrant transition,^{20,30} where not only the lateral segment density profiles become homogeneous but also the cylinder backbones loose their lamellar order, and a truly fluid monolayer is formed.

Conclusion

Monolayers of polymacromonomers with poly(vinyl)pyridine side chains of different length, polyPVP_{20.8} and polyPVP_{46.7}, are studied at the air–water surface. It is shown that the phase existing at pressures between 0 and ca. 15 mN/m, distinguished by a rather low compressibility, consists of aligned single molecules.

Two peaks in the GID data of the expanded phase suggest lateral order in the film. The common approach to calculate GID data based on atoms or pseudoatoms (consisting of groups of atoms) is useless in the case of polymacromonomer monolayers. Instead, a description on the base of the laterally periodic electron density profile is derived. By this means, a structural model has been established, which is consistent with the reflection and GID data and allows a quantitative description of the latter.

The reflection data of the expanded phase indicate pronounced side chain adsorption to the air–water interface. The proposed model of the expanded phase consists of a slightly curved polymacromonomer/air interface (on the order of few Å) and an elongated blob/brush-like structure protruding from the backbone into the aqueous subphase. The resulting electron density variations correspond to the peaks observed experimentally in the rod-scans. Due to the high electron density variation at the air/monolayer interface, the corresponding peak in $\tilde{\rho}(z)$ is sharp and intense. In contrast, the peak in $\tilde{\rho}(z)$ due to the molecule/subphase interface is rather broad and weak, features which are attributed to the extended side chains directly beneath the backbone and to the small difference in the electron density provided by polymer and water, respectively. The maximum cylinder backbone separation corresponds to twice the contour length of the side chains (25 and 12.5 nm, respectively) and decreases on monolayer compression by approximately 20%.

Approaching the phase transition at 15 mN/m, the correlation length decreases. Above the phase transition, the isotherms exhibit a very large compressibility. No lateral order could be detected, obviously the side chains of different molecules touch and mix. On compression, the cylinders thicken further. For the cylinders with long side chains, the phase transition from single aligned molecules to homogeneous monolayers is likely to be a reentrant transition.

The less side chains are adsorbed in the expanded phase, the smaller the intracylinder forces are which cause molecular stretching. The phase transition occurs when the backbone desorbs from the interface, and the side chains from different

molecules interpenetrate and mix. Therefore, the phase transition is caused not only by intermolecular interactions as is known from polymers with a simple architecture, but by intramolecular interactions, too.

Acknowledgment. We are deeply grateful to Kristian Kjaer for his continuous help with the liquid surface spectrometer at BW1, especially with the alignment of the slits before the soller and his prompt support with those problems, which arise suddenly out of thin air. We thank Peter Dziezok and Tim Stephan for providing us with the polymer samples. The Langmuir trough with enclosure used during the experiments was a generous loan by Mathias Lösche and Peter Krüger, and their help is appreciated. Discussions with Hartmut Löwen on reentrant phase transitions were illuminating. We thank HASYLAB, DESY (Hamburg, Germany) for synchrotron beamtime at the BW1 line and support. The financial support of the Schwerpunkt "Benetzung" (He 1616/9-2,3,4) is gratefully acknowledged, as well as the support of the state Mecklenburg-Vorpommern.

References and Notes

- (1) Ahrens, H.; Baekmark, T. R.; Merkel, R.; Schmitt, J.; Graf, K.; Raiteri, R.; Helm, C. A. *ChemPhysChem* **2000**, *1*, 101–106.
- (2) Ahrens, H.; Förster, S.; Helm, C. A. *Phys. Rev. Lett.* **1998**, *81*, 4172–4175.
- (3) Ahrens, H.; Graf, K.; Helm, C. A. *Langmuir* **2001**, *17*, 3113–3115.
- (4) Ahrens, H.; Hugenberg, N.; Schmidt, M.; Helm, C. A. *Phys. Rev. E* **1999**, *60*, 4360–4370.
- (5) Albrecht, O.; Gruler, H.; Sackmann, E. *J. Phys. (Paris)* **1978**, *39*, 301–313.
- (6) Als-Nielsen, J.; Kjaer, K. X-ray reflectivity and diffraction studies of liquid surfaces and surfactant monolayers. In *Phase Transitions of Soft Condensed Matter*; Sherrington, T. R. a. T., Ed.; Plenum Press: New York, 1989; Vol. 211, pp 113–137.
- (7) Als-Nielsen, J.; Möhwald, H. Synchrotron X-ray scattering studies of Langmuir films. In *Handbook of Synchrotron Radiation*; Ebashi, S., Rubenstein, E., Koch, M., Eds.; North-Holland: Amsterdam, 1989; Vol. 5, pp 1–53.
- (8) Asmussen, A.; Riegler, H. *J. Chem. Phys.* **1996**, *104*, 8159–8164.
- (9) Baltes, H.; Schwendler, M.; Helm, C. A.; Möhwald, H. *J. Colloid Interface Sci.* **1996**, *178*, 135–143.
- (10) Beer, M.; Schmidt, M.; Muthukumar, M. *Macromolecules* **1997**, *30*, 8375–8385.
- (11) Chen, Y. L.; Helm, C. A.; Israelachvili, J. N. *J. Phys. Chem.* **1991**, *95*, 10736–10747.
- (12) Evans, D. F.; Wennerström, H. *The Colloidal Domain: Where Physics, Chemistry, Biology, and Technology Meet*; VCH: Weinheim, Germany, 1994.
- (13) Hecht, E. *Optics*; Addison-Wesley: Reading, PA, 1990.
- (14) Helm, C. A.; Möhwald, H.; Kjaer, K.; Als-Nielsen, J. *Biophys. J.* **1987**, *52*, 381–391.
- (15) Israelachvili, J. N. *Intermolecular and Surface Forces*, 2nd ed.; Academic Press: London, 1991.
- (16) Kjaer, K.; Als-Nielsen, J.; Helm, C. A.; Laxhuber, L. A.; Möhwald, H. *Phys. Rev. Lett.* **1987**, *58*, 2224–2227.
- (17) Kjaer, K.; Als-Nielsen, J.; Kenn, R.; Böhm, C.; Tippmann-Krayer, P.; Peterson, I. R.; Bibo, A.; Helm, C. A.; Möhwald, H.; Leveillier, F.; Jacquemain, D.; Weinbach, S.; Leiserowitz, L.; Deutsch, M. *Makromol. Chem., Macromol. Symp.* **1991**, *46*, 433–437.
- (18) Kuzmenko, I.; Rapoport, H.; Kjaer, K.; Als-Nielsen, J.; Weissbuch, I.; Lahav, M.; Leiserowitz, L. *Chem. Rev.* **2001**, *101*, 1659–1696.
- (19) Li, C.; Gunari, N.; Fischer, K.; Schmidt, M.; Janshoff, A. *Angew. Chem.* **2004**, *43*, 1101–1104.
- (20) Likos, C. N.; Hoffmann, N.; Jusufi, A.; Löwen, H. *J. Phys.: Condens. Matter* **2003**, *15*, 233–238.
- (21) Möhwald, H. *Rep. Prog. Phys.* **1993**, *56*, 653.
- (22) Müller-Buschbaum, P.; Gutmann, J. S.; Wolkenhauer, M.; Kraus, J.; Stamm, M.; Smilgies, D.; Petry, W. *Macromolecules* **2001**, *34*, 1369–1375.
- (23) Pedersen, J. S. *J. Appl. Crystallogr.* **1992**, *25*, 129–145.
- (24) Pedersen, J. S.; Hamley, I. W. *J. Appl. Crystallogr.* **1994**, *27*, 36–49.
- (25) Pershan, P. S.; Als-Nielsen, J. *Phys. Rev. Lett.* **1984**, *52*, 759.
- (26) Schwartz, D. K.; Schlossman, M. L.; Kawamoto, E. H.; Kellogg, G. J.; Pershan, P. S. *Phys. Rev. A* **1990**, *41*, 5687–5690.
- (27) Sheiko, S. S.; Möller, M. *Top. Curr. Chem.* **2001**, *212*, 137–175.
- (28) Sheiko, S. S.; Prokhorova, S. A.; Beers, K.; Matyjaszewski, K.; Potemkin, I. I.; Khokhlov, A. R.; Möller, M. *Macromolecules* **2001**, *34*, 8354–8360.
- (29) Simister, E. A.; Lee, E. M.; Thomas, R. K.; Penfold, J. *J. Phys. Chem.* **1992**, *96*, 1373.
- (30) Watzlawek, M.; Likos, C. N.; Löwen, H. *Phys. Rev. Lett.* **1999**, *82*, 5289–5292.